Variability of the Ross Gyre, Southern Ocean: drivers and responses revealed by satellite altimetry

Tiago S. Dotto[1], Alberto Naveira Garabato[1], Sheldon Bacon[2], Michel Tsamados[3], Paul R. Holland[4], Jack Hooley[1], Eleanor Frajka-Williams[1], Andy Ridout[3] and Michael P. Meredith[4]

[1] Ocean and Earth Science, University of Southampton, Southampton, UK

[2] National Oceanography Centre, Southampton, UK

[3] Centre for Polar Observation and Modelling, University College London, London, UK

[4] British Antarctic Survey, Cambridge, UK

Corresponding author: Tiago S. Dotto (tiagosdotto@gmail.com)

Key Points:

- Variability in Ross Gyre circulation is assessed using radar altimetry, including in ice-covered regions
- Ross Gyre area, strength and throughflow vary semiannually, in response to atmospheric forcing associated with the Amundsen Sea Low
- Accounting for sea ice drag is essential to understand the Ross Gyre's response to atmospheric forcing

Abstract

Year-round variability in the Ross Gyre (RG), Antarctica, during 2011-2015, is derived using radar altimetry. The RG is characterized by a bounded recirculating component, and a westward 'throughflow' to the south. Two modes of variability of the sea-surface height (SSH) and ocean surface stress curl are revealed. The first represents a large-scale SSH change forced by the Antarctic Oscillation. The second represents semiannual variability in gyre area and strength, driven by fluctuations in sea level pressure associated with the Amundsen Sea Low (ASL). Variability in the throughflow is also linked to the ASL. An adequate description of the oceanic circulation is achieved only when sea ice drag is accounted for in the ocean surface stress. The drivers of RG variability elucidated here have significant implications for our understanding of the oceanic forcing of Antarctic Ice Sheet melting, and for the downstream propagation of its ocean freshening footprint.

Plain Language Summary

The Ross Gyre is one of the main current systems of the Southern Ocean, and conveys heat toward the cold continental shelves of the Antarctic Pacific sector, thus impacting the stability of diverse ice shelves. Due to the seasonal sea ice cover, measurements are sparse and little is known about the variability of the gyre's circulation and its driving forces. Here we use satellite radar altimetry to generate new light on the Ross Gyre variability. Two key aspects are identified: (i) large-scale variability of the sea-surface height driven by the zonal winds that flow around Antarctica, and (ii) changes in area and strength of the gyre, which are linked to a regional center of low pressure that modulates the local meteorology and sea ice conditions. This

same pressure system regulates the strength of the coastal currents, which potentially impacts on the distribution of key oceanic properties toward the Ross Sea. The processes identified in this study have strong implications for our understanding of the oceanic forcing of Antarctic Ice Sheet melting, and for the downstream propagation of its ocean freshening footprint.

1. Introduction

The Ross Sea (RS; Fig. 1a), Antarctica, is a region where mixing of distinct water masses and complex interactions with the cryosphere lead to the production and export of dense water, with global-scale impacts (Orsi & Wiederwohl, 2009). This region is sensitive to climatic changes, and perturbations in the water mass transformations that it hosts influence the properties and quantity of Antarctic Bottom Water exported to the global thermohaline circulation (Jacobs & Giulivi, 2010; Schmidtko et al., 2014). Offshore lies the cyclonic Ross Gyre (RG; Fig. 1a), an important regional component of the Southern Ocean, which controls the proximity of the warm waters of the Antarctic Circumpolar Current (ACC) to the RS continental shelf, where they may drive ice-shelf melting (Rignot et al., 2013; Paolo et al., 2015) and increasing sea level (Rye et al., 2014). Recent estimates of RG strength from numerical models and inverse approaches suggest a recirculating transport of ~15-30 Sv (Chu & Fan, 2007; Mazloff et al., 2010; Nakayama et al., 2014), though this value varies among simulations (Wang, 2013). Due to the difficulty of measuring ice-covered regions, little is known about the RG variability.

Radar altimetry is an accurate tool for measuring changes in the surface ocean circulation. However, sea ice has hampered the assessment of sea level around Antarctica by remote sensing, limiting understanding of oceanic variability to ice-free periods (Rye et al., 2014). Measurement of sea-surface height (SSH) in ice-covered regions became feasible with the method of Peacock and Laxon (2004), in which the specular signal returned from sea ice leads is recovered. In the Arctic Ocean, radar altimetry has been widely used to assess the SSH variability and associated oceanic circulation (Giles et al., 2012; Bulczak et al., 2015; Armitage et al., 2016; Mizobata et al., 2016), providing a new perspective on that basin. Recently, Kwok & Morrison (2015) demonstrated the potential use of radar altimetry to study the ice-covered Southern Ocean, with

Armitage et al. (2018) showing that the large-scale wind curl modulates non-seasonal variability of austral SSH, including within the subpolar (Ross and Weddell) gyres.

Here, we assess the RG circulation using radar altimetry from CryoSat-2, to generate new insight into its seasonal and interannual variability and its forcing mechanisms.

2. Data and Methods

2.1. Altimetric data

Gridded along-track SSH measurements acquired by CryoSat-2 (Wingham et al., 2006) between November 2010 and February 2016 were used. CryoSat-2 operates in different modes in the Southern Ocean: Low-Resolution Mode (LRM) in the open ocean away from sea ice; Synthetic Aperture Radar (SAR) over sea ice; and SAR Interferometric (SARIN) in coastal regions. SSH data in ice-covered areas were processed following the method of Peacock and Laxon (2004), which distinguishes between specular echoes from leads and diffuse echoes from sea ice. Open-ocean SSH data were processed using standard techniques. A seasonal offset between the lead and open-ocean data was identified, caused by the different retrackers used to fit the altimeter return echoes; this was added back to the lead data to correct the bias (Giles et al., 2012; Bulczak et al., 2015; Armitage et al., 2016, 2018). The open-ocean bias between the SAR and LRM was corrected in the same way. The bias-corrected SSH was then referenced to the EGM2008 geoid (Pavlis et al., 2012) to create dynamic ocean topography (DOT). Use of a different geoid does not significantly affect our conclusion; see Supplementary Material. Along-track data $\pm 3\sigma$ from the mean were removed. The data were then binned onto a regular grid spacing 0.5˚ (latitude) by 1˚ (longitude), and smoothed with a 300-km radius Gaussian filter to

remove small-scale signals absent from the geoid. Zonal (u) and meridional (v) surface geostrophic currents were derived as $u = -(g/f)(d\eta/dy)$ and $v = (g/f)(d\eta/dx)$, where g is acceleration due to gravity, f is Coriolis parameter, η is DOT, and y and x are meridional and zonal distances. The estimated uncertainty for the gridded SSH is 1.5 cm (see Supplementary Material). Hereafter, we will refer to the DOT minus its 2011-2015-mean as SSH, and the errors shown are standard deviation (standard error) for the time-mean (annual cycle) estimates.

2.2. Investigation of drivers of Ross Gyre variability

Monthly wind stress, wind stress curl (WSC), ocean surface stress and ocean surface stress curl (OSC) were calculated. Wind data were obtained from ECMWF/ERA-Interim reanalysis (Dee et al., 2011). Sea ice concentration (SIC) data are from NSIDC (Cavalieri et al., 1996), and sea ice drift data are from the Polar Pathfinder Daily Sea Ice Motion (Tschudi et al., 2016). All datasets were linearly interpolated onto the SSH grid and restricted to the time period of January 2011 to December 2015, i.e. years with all months. The total ocean surface stress in each grid cell is:

$$\vec{\tau} = \alpha\vec{\tau}_{ice-water} + (1-\alpha)\vec{\tau}_{air-water}$$

where:

$$\vec{\tau}_{ice-water} = \rho_{water} C_{iw} \left|\vec{U}_{ice}\right| \vec{U}_{ice}$$

$$\vec{\tau}_{air-water} = \rho_{air} C_{d} \left|\vec{U}_{air}\right| \vec{U}_{air}$$

and α is SIC, ρ_{air} is 1.25 kg/m^3, ρ_{water} is 1028 kg/m^3, C_d and C_{iw} are, respectively, the air-water and ice-water drag coefficients set to 1.25×10^{-3} and 5.50×10^{-3} (Tsamados et al., 2014). Here,

we considered a constant C_{iw} and stagnant ocean as a first assessment of the leading-order impact of sea ice on ocean surface stress. A sensitivity test showed that our results are qualitatively independent of the chosen C_{iw} (Fig. S2).

The relation between SSH and OSC was assessed via Maximum Covariance Analysis (MCA) using singular value decomposition, whereby the covariance patterns of the cross-covariance matrix are extracted (Wallace et al., 1992). We conducted this analysis for January 2011 to December 2015, and geographic coordinates between 150˚-290˚E and south of 60˚S to span the ice-covered region. Both datasets had their means and linear trends subtracted.

Two climatic indices were used to evaluate the atmospheric large-scale influence over the RG: the Antarctic Oscillation (AAO, also known as Southern Annular Mode, SAM; Thompson & Wallace, 2000) and the Amundsen Sea Low (ASL; Hosking et al., 2016) indices. The AAO is a proxy for the strength of the mid-latitude Southern Ocean westerlies. The ASL is a semiannually-varying centre of low pressure located in the Amundsen Sea (Fig. 2a) that modulates a significant fraction of atmospheric and sea ice variability in West Antarctica (Turner et al., 2013). Relationships with other climatic indices (e.g., ENSO) were examined but found not significant, likely due to the relatively short time-span of the satellite dataset.

GRACE RL05-Mascon Ocean Bottom Pressure anomalies (OBP) from CSR (Save et al., 2016) were used to evaluate altimetric SSH and its barotropic component (Fig. S3). Hereafter, p-values are not given if the correlation coefficient is above the 99% confidence level.

2.3. Characterization of the Ross Gyre

Two key aspects of the RG circulation are examined: (i) the area and intensity of the gyre's recirculating component, and (ii) the westward near-slope flow (hereafter, 'throughflow') adjacent to the RG recirculation cell. This current is important in exchanging waters between the ACC and the continental shelf of the RS (Orsi & Wiederwohl, 2009). The RG boundary was taken as the highest closed DOT contour in each month (Fig. 1b), following Foukal and Lozier (2017). The southern boundary of the ACC (sbACC) was defined as the -2 m DOT contour, which was the lowest contour that never intersects Antarctica, and coincides with a DOT gradient maximum (Fig. 1b). We estimated the gyre's barotropic transport (BT) assuming no vertical shear. Therefore, the BT overestimates the net transport of the RG, because available estimates suggest a baroclinic transport of *ca.* 8 Sv (Gouretski, 1999). Consequently, the BT likely also overestimates the transport variability, because the gyre's baroclinic structure is omitted (due to lack of subsurface measurements). However, comparison of SSH with gravity-derived OBP indicates that the barotropic mode dominates transport variability for the monthly-interannual timescales considered here (Fig. S3), so that the BT does generally characterise transport variability. We define BT as the maximum meridional integral of the vertically-integrated zonal velocity between the gyre's southern boundary and its centre, marked by the regional minimum in DOT (Wang, 2013). The throughflow was quantified as the monthly-mean zonal velocity across a section extending between the gyre's southern boundary and a point 100 km from the coast along 153˚W; this longitude is representative of the westward flow across 140˚-170˚W. Data close to the coast were excluded in this analysis due to geoid uncertainties (Fig. 1a).

3. Results

3.1. Recirculation within the Ross Gyre

SSH within the RG exhibits substantial month-to-month variability (Fig. 1c), with maxima of ~1.4±1 cm in August-November and minima of ~-3.5±0.7 cm in April (Fig. 1d). The RG time-mean area during the study period is ~1.84±0.47 × 10^6 km^2, and integrates strong semiannual and higher-frequency variability (Figs. 1e-f). The largest area is observed in May (~2.20±0.22 × 10^6 km^2) and November (~2.30±0.14 × 10^6 km^2), and the smallest at the end of winter and, most prominently, in summer (a decrease of ~36% from November). A clear areal decline is observed in 2015, when the RG spans ~0.80 × 10^6 km^2 in March-April (Fig. 1e). Area and SSH display a marginally significant correlation (r=0.41, p=0.05), suggesting a weak coupling between these features. The BT exhibits a time-mean of ~23±8 Sv, and large variability. A weakening of the gyre is observed in 2015 (Fig. 1g), concurrent to the reduction in area. RG strengthening is highly correlated with its expansion (r=0.84), pointing to common drivers. The mean seasonal cycle in gyre strength exhibits two periods of intensification, in May and November, when the BT peaks at ~30±4.6 Sv (Fig. 1h). Gyre weakening is observed in February (~17±2.8 Sv) and September (~18±2.9 Sv), a reduction of ~40% from May/November.

3.2. Throughflow

The RG throughflow may flow onto the continental shelf of the RS, or westward of Cape Adare (Fig. 1a). During the study period, the mean zonal throughflow is ~4.3±0.8 cm s^{-1} (Fig. 1i). Its variability of 0.8 cm s^{-1} corresponds to a barotropic transport of ~6 Sv, based on a mean depth of 4000 m and a mean distance of 200 km (Fig. 1b). Extreme maxima and minima of ~6.3 cm s^{-1} and ~2.7 cm s^{-1} occurred in April 2012 and September 2015, respectively. The mean seasonal cycle displays a peak velocity of ~4.8±0.5 cm s^{-1} in April-May. From May to October, velocity decreases by ~19%, reaching a minimum of ~3.9±0.4 cm s^{-1}, similar to summer values.

177 A second intensification of the throughflow occurs in November, when the zonal velocity rises to
178 ~4.6±0.1 cm s^{-1}.

179 **4. Discussion**

180 Radar altimetry captures well many features of the ice-covered RG, including its mean
181 position (160˚E-140˚W, south of the sbACC, and constrained by topography) and eastern
182 boundary at 140˚W (Gouretski, 1999; Chu & Fan, 2007). Near the RS shelf break, observed
183 geostrophic speeds are ~1-2 cm s^{-1}, increasing to >3-4 cm s^{-1} around Cape Adare and Cape
184 Colbeck (Fig. 1a), in agreement with modelling studies (Assmann et al., 2003; Padman et al.,
185 2009; Rickard et al., 2010). The ~23±8 Sv time-mean BT is within the range of previous
186 estimates of ~15-30 Sv (Chu & Fan, 2007; Mazloff et al., 2010; Nakayama et al., 2014). The
187 semiannual cycle of the RG (Fig. 1f,h) endorses model-based predictions, which suggested low
188 (high) volume/strength in solstitial (equinoctial) periods (e.g., Dellnitz et al., 2009; Duan et al.,
189 2016) in response to wind forcing.

190 Across the Southern Ocean, wind plays the main role in controlling SSH variability on the
191 timescales considered here (Gill & Niiler, 1973; Vivier et al., 2005). However, local sea-ice
192 cover impacts momentum transfer to the ocean (Tsamados et al., 2014; Martin et al., 2014), and
193 may modulate the oceanic response (Kim et al., 2017). To examine the atmospheric and sea ice
194 forcings on RG dynamics, we performed a MCA using SSH and OSC for 2011-2015 over the
195 West Antarctic sector.

196 The first MCA mode (MCA1), which explains 47% of the squared covariance between SSH
197 and OSC (Fig. 2a-b), identifies a large-scale structure extending from the ice-covered regions

toward the Southeast Pacific between 90˚-150˚W (also represented by the first EOF mode of SSH, Fig. S4). MCA1 represents the effect of Ekman pumping associated with wind-induced ocean stress on SSH variability, because OSC-driven convergence (divergence) of the local Ekman transport induces an increase (decrease) of SSH. Both principal components of MCA1 (PC1) are strongly coupled (r=0.80) and correlate with RG SSH (r=0.87 and r=0.64 for SSH PC1 and OSC PC1, respectively), and with the AAO index (r=-0.62 and r=-0.54, respectively; Fig. 2c). This suggests that sea level variability in the West Antarctic sector, including the RG, is regulated by large-scale meridional Ekman transport forced by circumpolar zonal winds, which removes (adds) mass from (to) the coastal region (Vivier et al., 2005; Armitage et al. 2018). South of the RG, the MCA1 patterns (Fig. 2a-b) display opposite spatial footprints, although this does not affect RG SSH. The cause of this feature is unclear, and its occurrence is sensitive to the choice of C_{iw}.

The second MCA mode (MCA2), which explains 30% of the squared covariance between SSH and OSC (Fig. 2d-e), contrasts the coastal and open-ocean regions (also seen in the second EOF mode; Fig. S4). Both principal components of MCA2 (PC2) are coupled (r=0.80; Fig. 2f). The coastal signal (Fig. 2d) is identified as the “southern mode” (Hughes et al., 1999; Aoki, 2002; Kusahara & Oshima, 2009)—a band of coherent oceanic pressure variability around Antarctica forced by circumpolar winds that is challenging to extract from conventional altimetry due to sea-ice cover (Hughes & Meredith, 2006). The Southeast Pacific signal (100˚-130˚W; Fig. 2d) is seemingly an extension of the barotropic “almost-free” mode (Webb & de Cuevas, 2003; Weijer, 2015) resulting from wind-induced mass convergence/divergence (Boening et al., 2011; Ponte & Piecuch, 2014). This mode is intensified during 2015—a year of exceptional El Niño conditions (Santoso et al., 2017).

221 The patterns represented by MCAs are large-scale manifestations relative to the domain. In
222 the MCA2, for instance, those representations stem from the low-pressure system centred in the
223 Amundsen-Bellingshausen Seas (Cohen et al. 2013; Fig. 2), which receives forcing from ENSO
224 and AAO/SAM via atmospheric teleconnections (Yuan, 2004; Clem et al. 2017). Propagation of
225 atmospheric planetary waves from the tropics affects the regional sea level pressure (SLP) and
226 atmospheric circulation (Yuan, 2004; Steig et al. 2012; Dutrieux et al. 2014; Turner et al. 2017).
227 Whereas many works have addressed large-scale controls on the ASL (e.g., Turner et al. 2013;
228 Raphael et al. 2016), none have to date discussed the connections and responses between the
229 ASL and RG.

230 MCA2 correlates with changes in RG area ($r=0.69$ for SSH PC2 and $r=0.56$ for OSC PC2)
231 and BT ($r=0.61$ for SSH PC2 and $r=0.51$ for OSC PC2). Both PC2's are related to the ASL index
232 ($r=-0.47$, $p<0.05$ for SSH PC2; and $r=-0.62$, $p<0.01$ for OSC PC2; Fig. 2f). This suggests that the
233 ASL contributes to regulating the RG variability represented by the MCA2 (i.e. the gyre's area
234 and strength). Periods when the RG is larger and intensified are associated with a cyclonic
235 atmospheric circulation (negative OSC/SLP) anomaly over the Southeast Pacific/Amundsen-
236 Bellingshausen Seas, likely strengthened during La Niña condition (Dutrieux et al. 2014). Ekman
237 transport divergence induces a relative reduction of the SSH north of the gyre (Fig. 4), enabling
238 its outer boundary to move/expand northeastward (Fig. S5). Only small changes are observed in
239 the southern and northern boundaries of the gyre because of topographic constraints. Further, the
240 anomalous cyclonic forcing enhances westward surface stress along the RS shelf break, and
241 thereby accelerates the gyre's southern limb, resulting in a coupling between area and BT. The
242 converse RG response is observed for anomalous anticyclonic forcing, as in 2015 when the gyre
243 contracted and weakened (Fig. 1e,g) likely in association with El Niño (Santoso et al., 2017).

MCA2 also illuminates the controls of throughflow circulation, and is correlated with the throughflow magnitude ($r=0.57$, $p<0.01$ and $r=0.47$, $p<0.05$ for SSH PC2 and OSC PC2, respectively). The throughflow's drivers are most clearly illustrated by composites of anomalies in OSC, ocean surface stress and SLP for periods of elevated (Fig. 3a) and reduced (Fig. 3b) westward velocity, based on $\pm 1\sigma$ (Fig. 1i). When the throughflow is anomalously strong, a negative SLP anomaly between the Antarctic Peninsula and ~140˚W is developed, which generates a cyclonic circulation that intensifies westward surface stress along the continental shelf, and thereby promotes a southward Ekman transport anomaly (Fig. 3a), raising the SSH along the coast (not shown). Consequently, the pressure gradient between the continental shelf and slope increases, leading to a geostrophic acceleration of the throughflow. Periods of anomalously weak throughflow are characterized by opposite atmospheric and oceanic patterns (Fig. 3b). Those anomalies originating in the Bellingshausen Sea (Figs. 3a-b) follow *f/H* contours in accordance with barotropic "southern mode" dynamics (Hughes et al., 1999). This is in line with slope current variability elsewhere around Antarctica (Núñez-Riboni & Fahrbach, 2009; Mathiot et al., 2011), although baroclinic effects may also be substantial (Kim et al., 2016). The throughflow and BT correlate at $r=0.49$, indicating a significant level of covariance. Both circulation components are invigorated by anomalous cyclonic forcing in the Amundsen Sea.

The Amundsen Sea has hosted dramatic changes in melting of its floating ice shelves (Paolo et al., 2015) due to variable influx of warm deep waters onto the continental shelf (Rignot et al., 2013; Jenkins et al., 2016). This variability is thought to be primarily controlled by zonal winds modulating currents along the shelf break (Thoma et al., 2008). Wind-induced Ekman pumping may also influence the depth of the on-shelf thermocline and affect melt rates (Dutrieux et al., 2014; Kim et al., 2017; Christie et al. 2018). These processes agree with those documented here,

267 not least in their association with the ASL. Although the ASL's dominant feature is variability, it
268 has also experienced a deepening trend during autumn (Turner et al., 2013). This variability and
269 trend will affect the throughflow, which transports freshwater from the Amundsen Sea toward
270 and beyond the RS (Nakayama et al., 2014), with consequences for the regional budgets of heat
271 and freshwater and for dense water formation (Jacobs & Giulivi, 2010). Our findings also
272 suggest that the RG responds to the ASL forcing, and a future deepening of this feature might
273 expand and intensify the gyre, in accord with climate models (Meijers et al., 2012) and sea ice
274 drift trends (Holland & Kwok, 2012).

275 Finally, we note that a realistic representation of wind momentum transfer into the ocean was
276 only achieved when we accounted for sea-ice cover over the RG (Fig. S6-S8). An enhancement
277 of sea-ice concentration partially damps the wind momentum transfer into the ocean, especially
278 as sea ice drift reduces toward the coast. This leads to a positive OSC anomaly under ice-covered
279 areas (Fig. S8). Thus, two key points were better represented by the OSC than the WSC: (i)
280 convergence within the RG during winter, which explains the increase of SSH (Fig. S6); and (ii)
281 convergence along the Antarctic continental shelf, which intensifies the throughflow (Figs. 3a,
282 S7-8). Therefore, sea-ice cover must be considered to achieve an adequate representation of the
283 surface stress, and thus to elucidate the changing forcing on the ocean and its response.

284 **5. Conclusions**

285 Radar altimetry is used to investigate RG variability from November 2010 to February 2016.
286 SSH variability is dominated by a large-scale barotropic response to OSC anomaly forced by the
287 AAO (Fig. 2), showing minimum (maximum) sea level during late summer/early autumn
288 (winter/spring). Conversely, gyre area and strength vary with a semiannual cycle forced by the

289 ASL. The deepening of SLP over the Southeast Pacific/Amundsen-Bellingshausen Seas
290 generates a cyclonic circulation cell that reduces SSH north of the RG via Ekman divergence
291 (Fig. 4). The relative reduction of SSH to the north facilitates a northeastward expansion of the
292 gyre's outer boundary. Further, the gyre is intensified by a westward ocean stress anomaly over
293 its southern boundary. The ensuing southward Ekman transport anomaly raises SSH over the
294 continental shelf, and accelerates the westward throughflow by increasing the cross-slope
295 pressure gradient. The SLP centre may have greater impact over the RG transport or the
296 throughflow, depending on its location and strength.

297 Our study is necessarily limited to ocean surface currents; however, we have shown that
298 significant new understanding of ocean dynamics in ice-covered regions can be attained, with
299 implications for future climatic changes (Holland & Kwok, 2012; Rye et al., 2014). It is
300 important that continuity of radar altimeter missions is achieved, in order to fully exploit the
301 techniques used here and gain insights over longer periods. Finally, concurrent subsurface
302 measurements are a high priority to elucidate the relationships between surface circulation
303 changes and the transports of heat and other key properties in the interior of the ocean (Jacobs &
304 Giulivi, 2010).

305

Acknowledgements

The CryoSat-2 data were obtained from the European Space Agency (https://earth.esa.int/web/guest/data-access/) and processed at CPOM (UCL). The NASA Team ice concentration and Sea Ice Drift data are available from the National Snow and Ice Data Center at http://nsidc.org/data/nsidc-0051 and http://nsidc.org/data/nsidc-0116, respectively. ERA-Interim data are available from ECMWF (http://apps.ecmwf.int/datasets/data/interim-full-daily/levtype=sfc/). The AAO index is available from NOAA/CPC (http://www.cpc.ncep.noaa.gov/products/precip/CWlink/daily_ao_index/aao/aao.shtml). GRACE data are available from CSR (http://www2.csr.utexas.edu/grace/RL05_mascons.html). The ASL index is available from http://www.antarctica.ac.uk/data/absl/. We thank T. W. K. Armitage for initial assistance with the altimetric dataset. T. S. Dotto acknowledges support by the CNPq/Brazil PhD scholarship grant number 232792/2014-3. The participation of A. C. Naveira Garabato was supported by the Royal Society and the Wolfson Foundation, and that of M. P. Meredith by NERC via award NE/N018095/1. Geostrophic current data presented in this manuscript can be accessed via http://www.cpom.ucl.ac.uk/dynamic_topography.

References

Aoki, S. (2002). Coherent sea level response to the Antarctic Oscillation. *Geophysical Research Letters*, 29(20), 1950, https://doi.org/10.1029/2002GL015733.

Armitage, T.W.K., Bacon, S., Ridout, A.L., Thomas, S.F., Aksenov, Y., & Wingham, D.J. (2016). Arctic sea surface height variability and change from satellite radar altimetry and GRACE, 2003–2014. *Journal of Geophysical Research: Oceans, 121*, 4303–4322, https://doi.org/10.1002/2015JC011579.

328 Armitage, T.W.K., Kwok, R., Thompson, A.F. & Cunningham, G. (2018). Dynamic topography and sea
329 level anomalies of the Southern Ocean: Variability and teleconnections. *Journal of Geophysical*
330 *Research: Oceans, 123*, https://doi.org/10.1002/2017JC013534.

331 Assmann K., Hellmer, H.H. & Beckmann, A. (2003). Seasonal variation in circulation and water mass
332 distribution on the Ross Sea continental shelf. *Antarctic Science, 15(1)*, 3–11.
333 https://doi.org/10.1017/S0954102003001007.

334 Boening, C., Lee, T. & Zlotnicki, V. (2011). A record-high ocean bottom pressure in the South Pacific
335 observed by GRACE. *Geophysical Research Letters, 38*, L04602,
336 https://doi.org/10.1029/2010GL046013.

337 Bulczak, A.I., Bacon, S., Naveira Garabato, A.C., Ridout, A., Sonnewald, M.J.P., & Laxon, S.W. (2015).
338 Seasonal variability of sea surface height in the coastal waters and deep basins of the Nordic Seas,
339 *Geophysical Research Letters, 42*, 113–120, https://doi.org/10.1002/2014GL061796.

340 Cavalieri, D.J., Parkinson, C.L., Gloersen, P., & Zwally, H.J. (1996), updated yearly. Sea Ice
341 Concentrations from Nimbus-7 SMMR and DMSP SSM/I-SSMIS Passive Microwave Data, Version 1.
342 [2010–2016, 50–90°S, 140°E–70°W], Boulder, Colorado USA. *NASA National Snow and Ice Data*
343 *Center Distributed Active Archive Center*. http://dx.doi.org/10.5067/8GQ8LZQVL0VL. (last access: 30
344 June 2017).

345 Chu, P.C. & Fan, C. (2007). An inverse model for calculation of global volume transport from wind and
346 hydrographic data. *Journal of Marine Systems, 65(1–4)*, 376–399,
347 https://doi.org/10.1016/j.jmarsys.2005.06.010.

348 Clem, K.R., Renwick, J.A. & McGregor, J. (2017). Large-Scale Forcing of the Amundsen Sea Low and
349 Its Influence on Sea Ice and West Antarctic Temperature. Journal of Climate, 30, 8405–8424.
350 https://doi.org/10.1175/JCLI-D-16-0891.1.

351 Cohen, L., Dean, S., & Renwick, J. (2013). Synoptic Weather Types for the Ross Sea Region, Antarctica,
352 Journal of Climate, 26, 636–649. https://doi.org/10.1175/JCLI-D-11-00690.1.

353 Christie, F. D. W., Bingham, R. G., Gourmelen, N., Steig, E. J., Bisset, R. R., Pritchard, H. D., Snow, K.,
354 & Tett, S. F. B. (2018). Marie Byrd Land glacier change driven by inter-decadal climate-ocean
355 variability, The Cryosphere Discussion, in review. https://doi.org/10.5194/tc-2017-263.

Dee, D.P., Uppala, S.M., Simmons, A.J., Berrisford, P., Poli, P., et al. (2011). The ERA-interim reanalysis: Configuration and performance of the data assimilation system. *Quarterly Journal of the Royal Meteorological Society, 137(656),* 553–597. https://doi.org/10.1002/qj.828.

Dellnitz M, Froyland G., Horenkamp C., Padberg-Gehle, K., & Sen Gupta, A. (2009). Seasonal variability of the subpolar gyres in the Southern Ocean: a numerical investigation based on transfer operators. *Nonlinear Processes in Geophysics, 16(6)*, 655–663, https://doi.org/10.5194/npg-16-655-2009.

Duan Y., Liu, H., Yu, W. & Hou, Y. (2016). The mean properties and variations of the Southern Hemisphere subpolar gyres estimated by Simple Ocean Data Assimilation (SODA) products. *Acta Oceanologica Sinica, 35(7)*, 8–13, https://doi.org/10.1007/s13131-016-0901-2

Dutrieux, P., De Rydt, J., Jenkins, A., Holland, P.R., Ha, H.K., Lee, S.H., Steig, E.J., Ding, Q., Abrahamsen, E.P., & Schröder, M. (2014). Strong sensitivity of Pine Island Ice-Shelf melting to climatic variability. *Science, 343(6167)*, 174–178, https://doi.org/10.1126/science.1244341.

Foukal, N.P., & Lozier, M.S. (2017). Assessing variability in the size and strength of the North Atlantic subpolar gyre. *Journal of Geophysical Research: Oceans, 122*, 6295–6308, https://doi.org/10.1002/2017JC012798.

Giles, K.A., Laxon, S.W., Ridout, A.L., Wingham, D.J., & Bacon, S. (2012). Western Arctic Ocean freshwater storage increased by winddriven spin-up of the Beaufort Gyre. *Nature Geoscience, 5*, 194–197, https://doi.org/10.1038/ngeo1379.

Gill, A., & Niiler, P. (1973). The theory of the seasonal variability in the ocean. *Deep-Sea Research and Oceanographic Abstracts, 20*, 141–177, https://doi.org/10.1016/0011-7471(73)90049-1

Gordon, A.L., Huber, B.A., & Busecke, J. (2015). Bottom water export from the western Ross Sea, 2007 through 2010, Geophysical Research Letters, 42, 5387–5394, https://doi.org/10.1002/2015GL064457.

Gouretski, V. (1999). The large-scale thermohaline structure of the Ross Gyre. In: G. Spezie & G.M.R. Manzella (Eds.), *Oceanography of the Ross Sea Antarctica*. Springer, Milano, 77–100.

Holland, P.R., & Kwok, R. (2012). Wind-driven trends in Antarctic sea-ice drift. *Nature Geoscience, 5*, 872–875. https://doi.org/10.1038/ngeo1627

382 Hosking, J.S., Orr, A., Bracegirdle, T.J., & Turner, J. (2016). Future circulation changes off West
383 Antarctica: Sensitivity of the Amundsen Sea Low to projected anthropogenic forcing. *Geophysical*
384 *Research Letters, 43*, 367–376. https://doi.org/10.1002/2015GL067143.

385 Hughes, C.W., Meredith, M.P., & Heywood, K.J. (1999). Wind driven transport fluctuations through
386 Drake Passage: A southern mode. *Journal of Physical Oceanography, 29*, 1971–1992.
387 https://doi.org/10.1175/1520-0485(1999)029<1971:WDTFTD>2.0.CO;2

388 Hughes, C.W. & Meredith, M.P. (2006). Coherent sea level fluctuations along the global continental
389 slope. *Philosophical Transactions of the Royal Society, London, 364*, 885-901.
390 https://doi.org/10.1098/rsta.2006.1744.

391 Jacobs, S.S., & Giulivi, C.F. (2010). Large multidecadal salinity trends near the Pacific-Antarctic
392 continental margin. *Journal of Climate, 23*, 4508–4524. https://doi.org/10.1175/2010JCLI3284.1

393 Jenkins, A., Dutrieux, P., Jacobs, S., Steig, E.J., Gudmundsson, G.H., Smith, J., & Heywood, K.J. (2016).
394 Decadal ocean forcing and Antarctic ice sheet response: Lessons from the Amundsen Sea. *Oceanography,*
395 *29(4)*, 106–117. https://doi.org/10.5670/oceanog.2016.103.

396 Kim, C.S., Kim, T.W., Cho, K.H., Ha, H.K., Lee, S.H., Kim, H.C., & Lee, J.H. (2016). Variability of the
397 Antarctic Coastal Current in the Amundsen Sea, *Estuarine, Coastal and Shelf Science, 181*, 123-133.
398 http://dx.doi.org/10.1016/j.ecss.2016.08.004.

399 Kim, T. W., Ha, H.K., Wåhlin, A.K., Lee, S.H., Kim, C.S., Lee, J.H., & Cho, Y.K. (2017). Is Ekman
400 pumping responsible for the seasonal variation of warm circumpolar deep water in the Amundsen Sea?.
401 *Continental Shelf Research, 132*, 38-48. https://doi.org/10.1016/j.csr.2016.09.005.

402 Kusahara, K. & Ohshima, K. I. (2009). Dynamics of the wind-driven sea level variation around
403 Antarctica. *Journal of Physical Oceanography*, 39, 658–674. https://doi.org/10.1175/2008JPO3982.1.

404 Kwok, R., & Morison, J. (2015). Sea surface height and dynamic topography of the ice-covered oceans
405 from CryoSat-2: 2011–2014. *Journal of Geophysical Research: Oceans, 121*, 674-692.
406 https://doi.org/10.1002/2015JC011357.

407 Martin, T., Steele, M., & Zhang, J. (2014). Seasonality and long-term trend of Arctic Ocean surface stress
408 in a model. *Journal of Geophysical Research: Oceans, 119*, 1723–1738.
409 https://doi.org/10.1002/2013JC009425.

Mathiot, P., Goosse, H., Fichefet, T., Barnier, B., & Gallée, H. (2011). Modelling the seasonal variability of the Antarctic Slope Current. *Ocean Science, 7(4)*, 455–470. https://doi.org/10.5194/os-7-455-2011.

Mazloff, M.R., Heimbach, P., Wunsch, C. (2010). An eddy-permitting Southern Ocean state estimate. *Journal of Physical Oceanography, 40*, 880–899. https://doi.org/10.1175/2009JPO4236.1

Meijers, A.J.S., Shuckburgh, E., Bruneau, N., Sallee, J.-B., Bracegirdle, T.J., & Wang, Z. (2012). Representation of the Antarctic Circumpolar Current in the CMIP5 climate models and future changes under warming scenarios. *Journal of Geophysical Research, 117*, C12008, https://doi.org/10.1029/2012JC008412.

Mizobata, K., Watanabe, E., & Kimura, N. (2016). Wintertime variability of the Beaufort gyre in the Arctic Ocean derived from CryoSat-2/SIRAL observations. *Journal of Geophysical Research: Oceans, 121*, 1685–1699. https://doi.org/10.1002/2015JC011218.

Nakayama, Y., Timmermann, R., Rodehacke, C.B., Schröder, M., & Hellmer, H.H. (2014). Modeling the spreading of glacial meltwater from the Amundsen and Bellingshausen Seas. *Geophysical Research Letters, 41*, 7942–7949. https://doi.org/10.1002/2014GL061600.

Núñez-Riboni, I., & Fahrbach, E. (2009). Seasonal variability of the Antarctic Coastal Current and its driving mechanisms in the Weddell Sea. *Deep Sea Research Part I: Oceanographic Research Papers, 56(11)*, 1927–1941. https://doi.org/10.1016/j.dsr.2009.06.005.

Orsi, A.H., & Wiederwohl, C.L. (2009). A recount of Ross Sea waters. *Deep-Sea Research II: Tropical Studies in Oceanography, 56*, 778–795. https://doi.org/10.1016/j.dsr2.2008.10.033.

Orsi, A.H., Whitworth, T., & Nowlin, W.D. (1995). On the meridional extent and fronts of the Antarctic Circumpolar Current. *Deep Sea Research Part I, 42(5),* 641–673. https://doi.org/10.1016/0967-0637(95)00021-W.

Padman, L., Howard, S.L., Orsi, A.H., & Muench, R.D. (2009). Tides of the north-western Ross Sea and their impact on dense outflows of Antarctic Bottom Water. *Deep-Sea Research II: Tropical Studies in Oceanography, 56*, 818–834. https://doi.org/10.1016/j.dsr2.2008.10.026.

Paolo, F.S., Fricker, H.A., & Padman, L. (2015). Volume loss from Antarctic ice shelves is accelerating, *Science, 348*, 327–331. https://doi.org/10.1126/science.aaa0940.

Pavlis, N. K., Holmes, S.A., Kenyon, S.C., & Factor, J.K. (2012). The development and evaluation of the Earth Gravitational Model 2008 (EGM2008). *Journal of Geophysical Research, 117*, B04406, https://doi.org/10.1029/2011JB008916.

Peacock, N.R., & Laxon, S.W. (2004). Sea surface height determination in the Arctic Ocean from ERS altimetry. *Journal of Geophysical Research, 109*, C07001. https://doi.org/10.1029/2001JC001026.

Ponte, R.M., & Piecuch, C.G. (2014). Interannual bottom pressure signals in the Australian–Antarctic and Bellingshausen basins. *Journal of Physical Oceanography, 44*, 1456–1465. https://doi.org/10.1175/JPO-D-13-0223.1

Raphael, M.N., Marshall, G.J., Turner, J., Fogt, R.L., Schneider, D., Dixon, D.A., Hosking, J.S., Jones, J. M. & Hobbs, W.R. (2016). The Amundsen Sea low: Variability, change, and impact on Antarctic Climate. *Bulletin of American Meteorological Society*, 97, 111–121. https://doi.org/10.1175/BAMS-D-14-00018.1.

Rickard, G.J., Roberts, M.J., Williams, M.J., Dunn, A., & Smith, M.H. (2010). Mean circulation and hydrography in the Ross Sea sector, Southern Ocean: representation in numerical models. *Antarctic Science, 22*, 533–558. https://doi.org/10.1017/S0954102010000246.

Rignot, E., Jacobs, S., Mouginot, J., & Scheuchl, B. (2013) Ice-Shelf Melting Around Antarctica. *Science, 341*, 266-270. https://doi.org/10.1126/science.1235798.

Rye, C.D., Naveira Garabato, A.C., Holland, P.R., Meredith, M.P., Nurser, A.J.G., Hughes, C.W., Coward, A.C., & Webb, D.J. (2014). Rapid sea-level rise along the Antarctic margins in response to increased glacial discharge. *Nature Geoscience, 7*, 732-735, https://doi.org/10.1038/Ngeo2230.

Santoso, A., McPhaden, M.J., & Cai, W. (2017). The defining characteristics of ENSO extremes and the strong 2015/2016 El Niño. *Reviews of Geophysics, 55*, 1079–1129. https://doi.org/10.1002/2017RG000560.

Save, H., Bettadpur, S., & Tapley, B.D. (2016). High resolution CSR GRACE RL05 mascons. *Journal of Geophysical Research: Solid Earth, 121*, 7547-7569. https://doi.org/10.1002/2016JB013007.

Schmidtko, S., Heywood, K.J., Thompson, A.F., & Aoki, S. (2014). Multidecadal warming of Antarctic waters. *Science, 346*, 1227–1231. https://doi.org/10.1126/science.1256117.

Steig, E.J., Ding, Q., Battisti, D.S. & Jenkins, A. (2012). Tropical forcing of Circumpolar Deep Water Inflow and outlet glacier thinning in the Amundsen Sea Embayment, West Antarctica. *Annals of Glaciology*, (53)60, https://doi.org/10.3189/2012AoG60A110

Thoma, M., Jenkins, A., Holland, D., & Jacobs, S. (2008). Modelling Circumpolar Deep Water intrusions on the Amundsen Sea continental shelf, Antarctica. Geophysical Research Letters, 35, L18602, https://doi.org/10.1029/2008GL034939.

Thompson, D.W.J., & Wallace, J.M. (2000). Annular modes in the extratropical circulation. Part I: Month-to-month variability. *Journal of Climate, 13*, 1000–1016. https://doi.org/10.1175/1520-0442(2000)013,1000:AMITEC.2.0.CO;2.

Tsamados, M., Feltham, D.L., Schroeder, D., Flocco, D., Farrell, S.L., Kurtz, N., Laxon, S.W., & Bacon, S. (2014). Impact of variable atmospheric and oceanic form drag on simulations of Arctic sea ice. *Journal of Physical Oceanography, 44*, 1329–1353. https://doi.org/10.1175/JPO-D-13-0215.1.

Tschudi, M., Fowler, C., Maslanik, J., Stewart, J.S., & Meier, W. (2016). Polar Pathfinder Daily 25 km EASE-Grid Sea Ice Motion Vectors, Version 3. [2010–2016, 50–90°S, 140°E–70°W]. Boulder, Colorado USA. NASA National Snow and Ice Data Center Distributed Active Archive Center. http://dx.doi.org/10.5067/O57VAIT2AYYY (last access: 27 June 2017).

Turner, J., Phillips, T., Hosking, J.S., Marshall, G.J., & Orr, A. (2013). The Amundsen Sea low. *International Journal of Climatology, 33*, 1818–1829. https://doi.org/10.1002/joc.3558.

Turner, J., Hosking, J. S., Bracegirdle, T. J., Phillips, T. & Marshall, G. J. (2017). Variability and trends in the Southern Hemisphere high latitude, quasi-stationary planetary waves. *International Journal of Climatology*, 37, 2325–2336. https://doi.org/10.1002/joc.4848

Vivier, F., Kelly, K.A., & Harismendy, M. (2005). Causes of largescale sea level variations in the Southern Ocean: Analyses of sea level and a barotropic model. *Journal of Geophysical Research, 110*, C09014, https://doi.org/10.1029/2004JC002773.

Wallace, J.M., Smith, C. & Bretherton, C.S. (1992). Singular Value Decomposition of Wintertime Sea Surface Temperature and 500-mb Height Anomalies. *Journal of Climate, 5*, 561–576. https://doi.org/10.1175/1520-0442(1992)005<0561:SVDOWS>2.0.CO;2.

Wang, Z. (2013). On the response of Southern Hemisphere subpolar gyres to climate change in coupled climate models. *Journal of Geophysical Research: Oceans, 118*, 1070–1086. https://doi.org/10.1002/jgrc.20111.

Webb, D.J. & de Cuevas, B.A. (2003). The region of large sea surface height variability in the southeast Pacific Ocean. *Journal of Physical Oceanography, 33*, 1044–1056. https://doi.org/10.1175/1520-0485(2003)033<1044:TROLSS>2.0.CO;2.

Weijer, W. (2015). Modal variability in the Southeast Pacific Basin: Energetics of the 2009 event. *Deep-Sea Research II: Tropical Studies in Oceanography, 114*, 3-11, https://doi.org/10.1016/j.dsr2.2012.10.002.

Wingham, D.J., Francis, C.R., Baker, S., Bouzinac, C., Brockley, D., Cullen, R., et al. (2006). CryoSat: A mission to determine the fluctuations in Earth's land and marine ice fields. *Advances in Space Research Series, 37*, 841–871. https://doi.org/10.1016/j.asr.2005.07.027.

Yuan, X. (2004). ENSO-related impacts on Antarctic sea ice: a synthesis of phenomenon and mechanisms. Antarctic Science, 16, 415–425. https://doi.org/10.1017/S0954102004002238

Figures Captions

Figure 1. (a) Time-mean DOT and geostrophic velocity (2011-2015). Mean positions of the RG (black) and the sbACC (red) identified in the present work. Green line is the sbACC from Orsi et al. (1995). Light (dark) gray thick line depicts time-mean 15% SIC for summer (winter). Thin gray lines are 1000, 3000 and 4500 m isobaths. Thick red line marks the throughflow section. (b) Time-mean DOT (2011-2015) overlaid by monthly RG (white) and sbACC (purple) contours. Time-mean RG, sbACC, SIC and bathymetry are depicted as in panel (a). (c) Monthly RG SSH and (d) its annual cycle. (e) Monthly RG area and (f) its annual cycle. (g) Monthly westward BT and (h) its annual cycle. (i) Monthly zonal throughflow and (j) its annual cycle. Circles (squares) markers in (j) denote periods of -1 (+1) standard deviation from the detrended mean used in the composite analysis (Fig. 3). Shades in the annual cycle panels are the standard error from the time series. Horizontal gray lines in (c) to (j) are the respective time-mean values.

Figure 2. (a) First SSH MCA pattern for 2011-2015. AS=Amundsen Sea; BS=Bellingshausen Sea. (b) First OSC MCA pattern. (c) SSH PC1 (black) and OSC PC1 (red) alongside AAO index (blue), all normalized to have unit variance. (d) Second SSH MCA pattern. (e) Second OSC MCA pattern. (f) SSH PC2 (black) and OSC PC2 (red) alongside ASL index (blue), all normalized to have unit variance. AAO and ASL indices are inverted. 2011-2015 averaged 15% SIC is represented by the thick gray line in MCA maps. Black thin lines represent 1000, 3000 and 4500 m isobaths. Squared covariance explained by each MCA mode is indicated in the legends of (a) and (d). Correlation coefficient and p-value between the PCs are depicted in (c) and (f). In (b) and (e), SLP anomaly is regressed onto the SSH PCs. Green (magenta) lines represent negative (positive) SLP every 1 hPa interval. Black thick line is 0 hPa.

Figure 3. Anomaly composites for periods of (a) strongest and (b) weakest throughflow (Fig. 1i). OSC pattern is shown by the colors, ocean surface stress by vectors, and SLP (hPa) by black lines. Time-mean 15% SIC (magenta) and isobaths of 1000 and 3000 m (gray) are depicted.

Figure 4. Schematic of the processes involved on the expansion and intensification of the RG and throughflow. A negative SLP anomaly is formed north of the Amundsen Sea Embayment, which generates a cyclonic circulation over the region. This lowers sea level to the north via Ekman dynamics, allowing a northeastward migration of the RG outer boundary. Further, a westward surface stress anomaly is created over the gyre's southern boundary, accelerating the RG. Southward Ekman transport piles water up over the continental shelf, increasing SSH and the cross-shelf pressure gradient, and thereby intensifying the throughflow.

Figure 1.

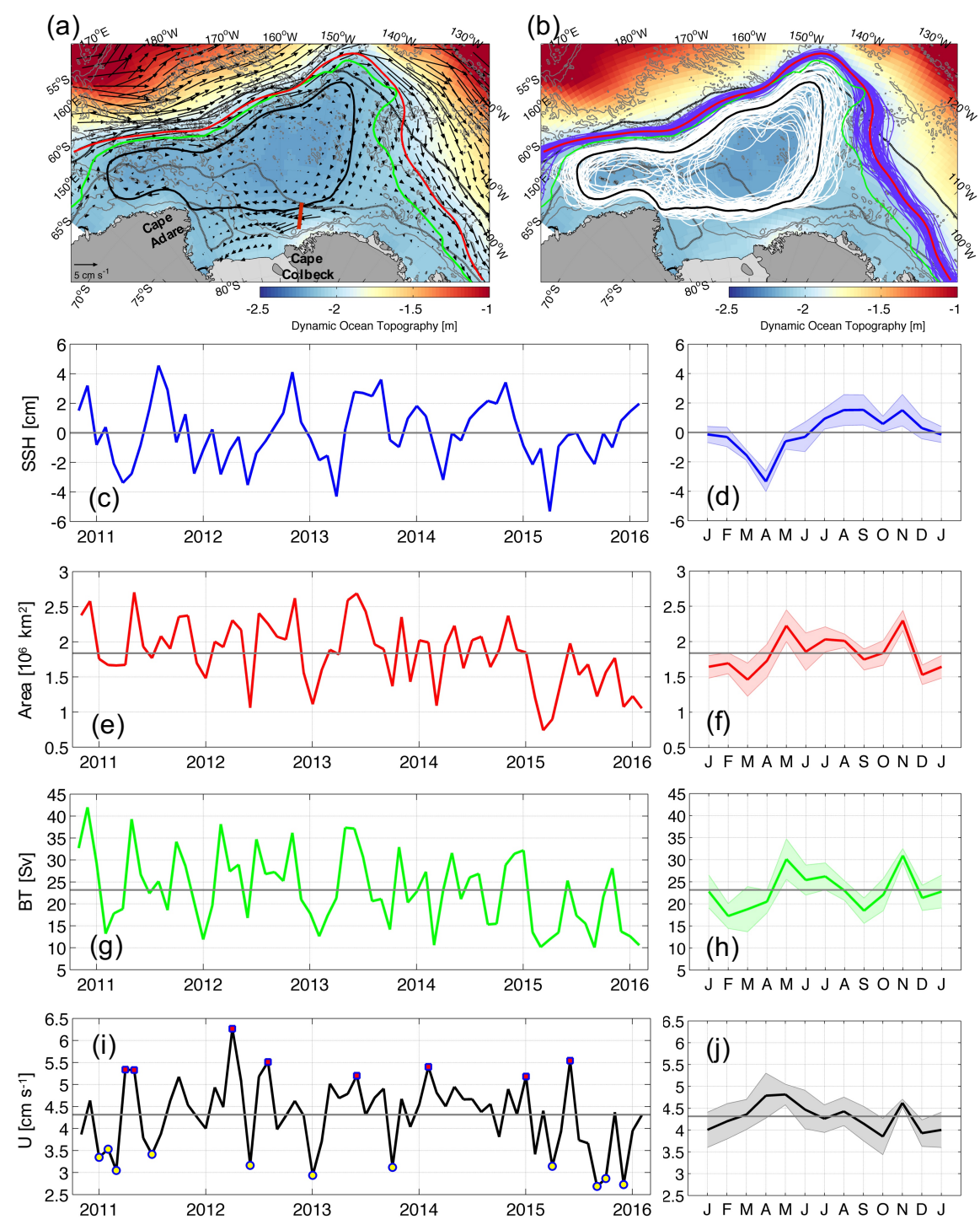
(a)
(b)
Cape Adare
Cape Colbeck
5 cm s⁻¹
Dynamic Ocean Topography [m]
SSH [cm]
(c)
(d)
Area [10⁶ km²]
(e)
(f)
BT [Sv]
(g)
(h)
U [cm s⁻¹]
(i)
(j)
J F M A M J J A S O N D J

Figure 2.

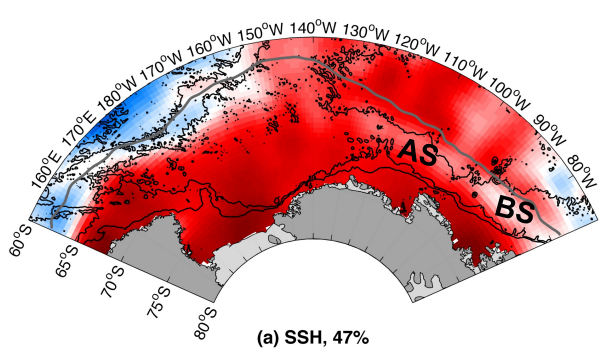

(a) SSH, 47%

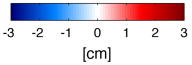

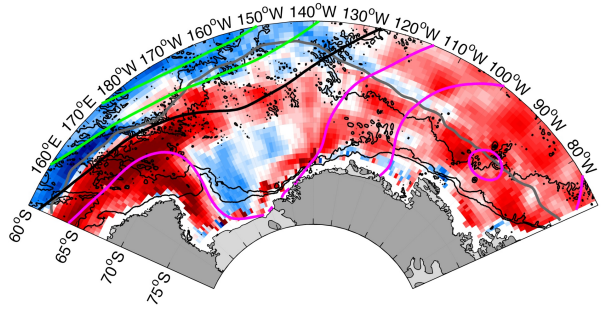

(b) Ocean Surface Stress Curl

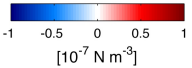

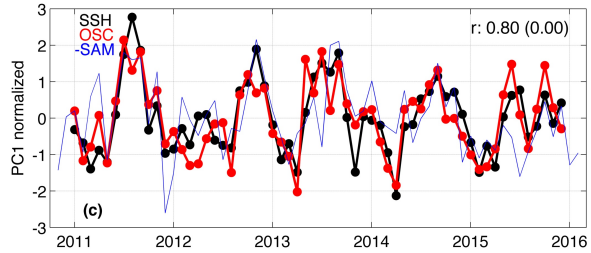

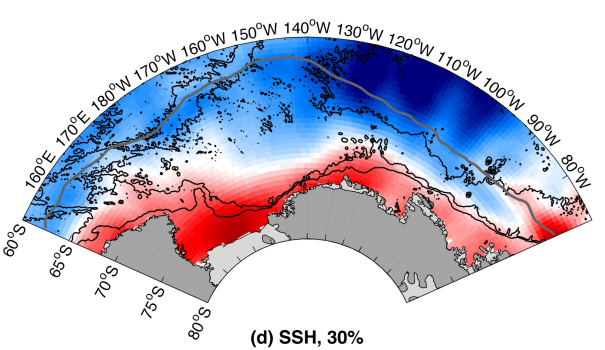

(d) SSH, 30%

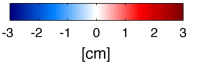

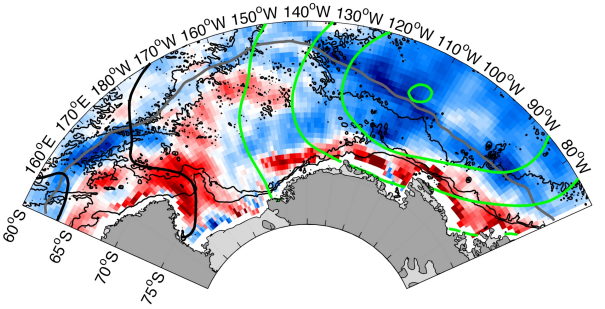

(e) Ocean Surface Stress Curl

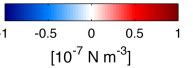

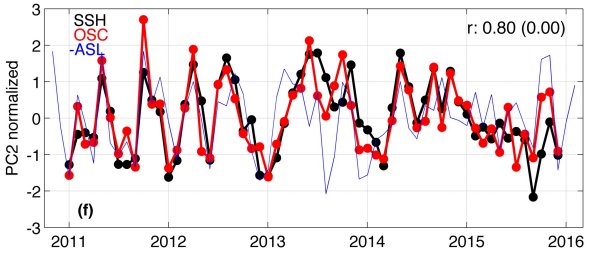

Figure 3.

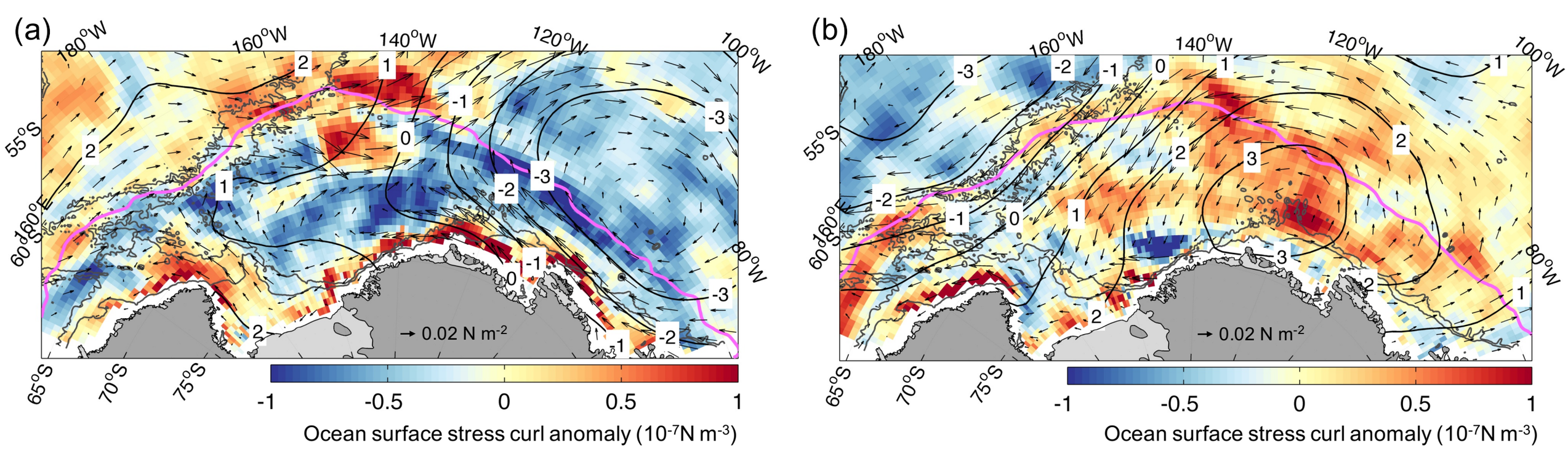
(a)
180°W
160°W
140°W
120°W
100°W
80°W
55°S
60°S
65°S
70°S
75°S
180°E
→ 0.02 N m-2
-1
-0.5
0
0.5
1
Ocean surface stress curl anomaly (10-7N m-3)
(b)
180°W
160°W
140°W
120°W
100°W
80°W
55°S
60°S
65°S
70°S
75°S
180°E
→ 0.02 N m-2
-1
-0.5
0
0.5
1
Ocean surface stress curl anomaly (10-7N m-3)

Figure 4.

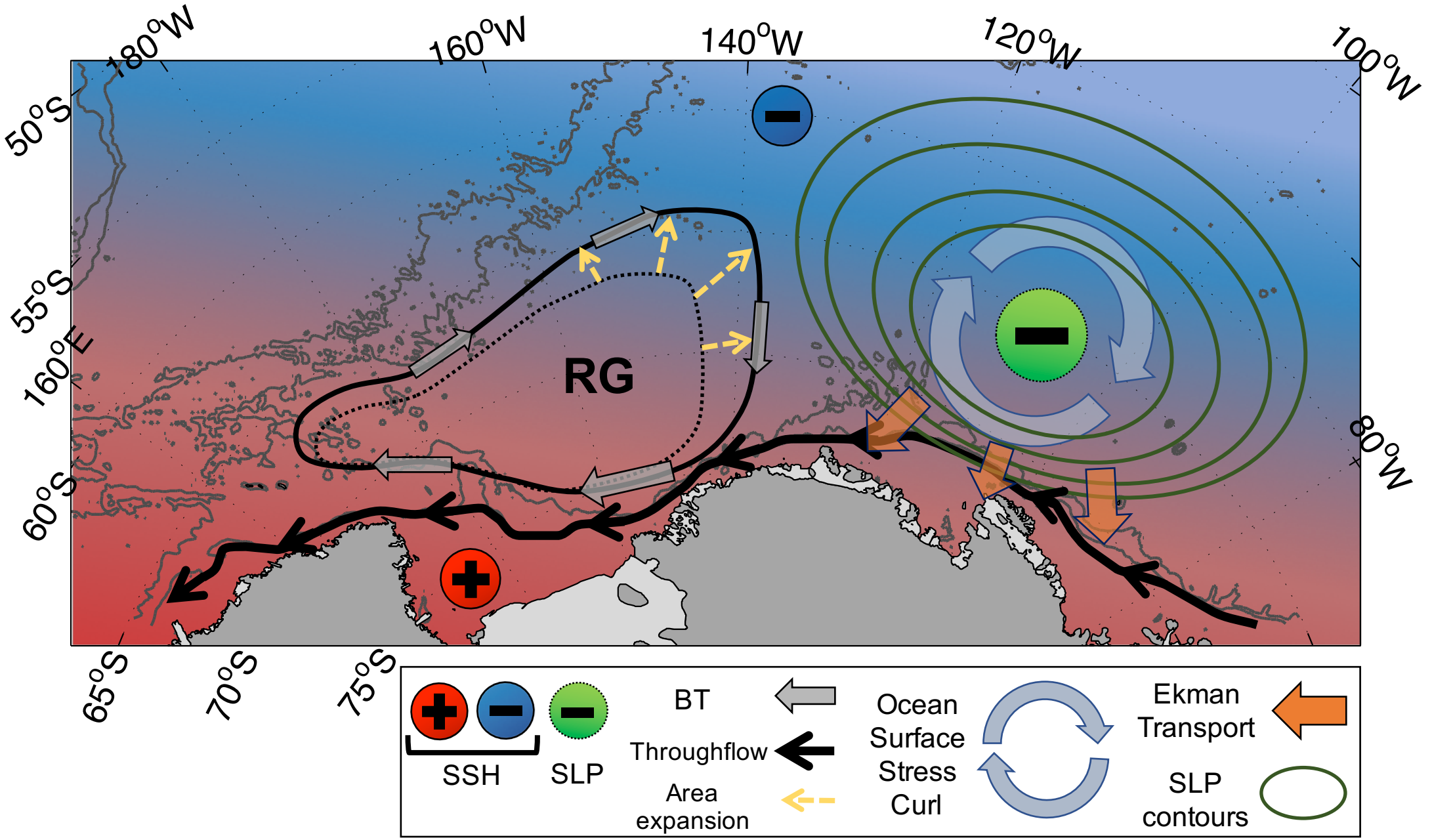
180°W
160°W
140°W
120°W
100°W
50°S
55°S
60°S
65°S
70°S
75°S
160°E
80°W
RG
SSH
SLP
BT
Throughflow
Area expansion
Ocean Surface Stress Curl
Ekman Transport
SLP contours